UCLA
UCLA Previously Published Works

Title

Fast Spectroscopic Gamma Scintillation Using Hafnium Oxide Nanoparticles—Plastic Nanocomposites

Permalink

https://escholarship.org/uc/item/8d02z8f5

Journal

Chemistry of Materials, 36(1)

ISSN

0897-4756

Authors

Yu, Hao

Winardi, Isabelle

Han, Ziqing

et al.

Publication Date

2024-01-09

DOI

10.1021/acs.chemmater.3c02631

Copyright Information

Peer reviewed

Fast Spectroscopic Gamma Scintillation Using Hafnium Oxide Nanoparticles-Plastic Nanocomposites

Hao Yu[a], Isabelle Winardi[a], Ziqing Han[a], David Prout[b,c], Arion Chatziioannou[b,c] and Qibing Pei[a,c]*

[a] Department of Materials Science and Engineering, University of California, Los Angeles,

420 Westwood Plaza, Los Angeles, CA, 90095, United States

[b] Crump Institute for Molecular Imaging, University of California, Los Angeles,
570 Westwood Plaza, Los Angeles, CA, 90095, United States

[c] California NanoSystems Institute, University of California, Los Angeles,

570 Westwood Plaza, Los Angeles, CA, 90095, United States

E-mail: qpei@seas.ucla.edu

ABSTRACT

Fast scintillators with spectroscopic gamma response are essential in nuclear security and medical imaging. However, few individual scintillation materials exhibit both fast scintillation decay and high photopeak energy resolution. We report a nanocomposite scintillator comprising 40 wt% of hafnium oxide nanoparticles uniformly dispersed in a luminescent plastic matrix. The nanoparticles have an average diameter of 4.2 nm and are covalently attached to the polymer matrix to prevent agglomeration and thus achieve high optical transparency across nanocomposite monoliths up to 8.5 mm thick. The measured transmittance is around 80% across the emission range. Gamma pulse scintillation has a fast decay time constant of 2.5 ns and high light output of 8,000- 9,000 photons/MeV. The gamma scintillation shows energy proportionality from 32 to 1275 keV. A 1.93 cm^3 nanocomposite produces photopeaks at 32 and 662 keV for ^{137}Cs, 511 and 1275 keV for ^{22}Na. The photopeak energy resolution at 662 keV is 7.2 %-9.1%.

Introduction

Scintillators are widely used in nuclear security, industrial screening, and medical imaging.[1] They offer efficient and convenient radiation detection by converting X/gamma rays to visible photons, which are detected by an external photomultiplier tube (PMT)/photodetector.[2] The detection of radioactive nuclear agents in ports involves high throughput screening of luggage/cargo for radioactive species in a conveyor with an enclosed volume of several cubic meters.[1] Large-size gamma scintillators with high light output are desired.[3] Gamma spectroscopy entails the capability of the scintillators to produce photopeaks with high energy resolution (ER) and the materials must have low natural radioactivity background.[1] In medical imaging, e.g. computed tomography (CT) and positron emission tomography (PET), fast scintillators can achieve high image quality while simplifying image reconstruction efforts.[4] Fast scintillators with a short rise time and decay time are desired for precise localization along the line of response in time-of-flight PET.[5] Only a few commercial scintillators, for example, LaBr$_3$:Ce and lutetium yttrium oxyorthosilicate (LYSO:Ce) have both fast scintillation decay (LaBr$_3$:Ce, 17 ns and LYSO:Ce, 40 ns) and good spectroscopic gamma response (ER at 662 keV being 2.6% for LaBr$_3$:Ce and 8-9 % for LYSO:Ce).[4] However, LaBr$_3$:Ce is very hygroscopic, requiring extra encapsulation for practical use, while lutetium (Lu) has high natural radioactivity background, making LYSO unsuitable for gamma spectroscopy.[1, 4]

Recent materials progress has shown promises to overcome these challenges. Two categories of single crystals have been developed, namely, two-dimensional hybrid organic-inorganic perovskite (HOIPs) crystals [6-9] and self-trapped exciton (STE) crystals.[10, 11] Jin et al. showed an ER at 662 keV of 21.7% and a decay constant of 7.9 ns for (PEA)$_2$PbBr$_4$ single crystals by suppressing the non-radiative defects in crystal growth.[9] Xie et al. used lithium doping in (BA)$_2$PbBr$_4$ single crystals and pushed the ER to 8% with a scintillation decay constant of 10.9

2

ns.[8] However, these 2D HOIP crystals favor in-plane growth, and thus the crystal thickness is usually restricted to only a few millimeters, which is rather small to attenuate high energy gamma photons.[7]

Meanwhile, STE crystals with various compositions have been developed. Burger et al. showed Cs_2HfCl_6 crystals with an exceptional ER of 3.3% at 662 keV and a scintillation decay constant of 4.37 μs.[10] Wang et al. reported a lithium doped $Cs_3Cu_2I_5$ single crystal having an ER of 4.8% at 662 keV with a decay constant of 949 ns.[11] While showing exceptional ER, STE crystals have long scintillation decay times due to the slow lattice relaxation and exciton transport.[12] To illustrate the scintillation performance of various emerging materials, scintillation decay constant and energy resolution at 662 keV are shown in **Figure 1**, with the scintillation parameters of these materials summarized in **Table S1**. An ideal fast spectroscopic scintillator material shall sit in the left bottom corner in the diagram.
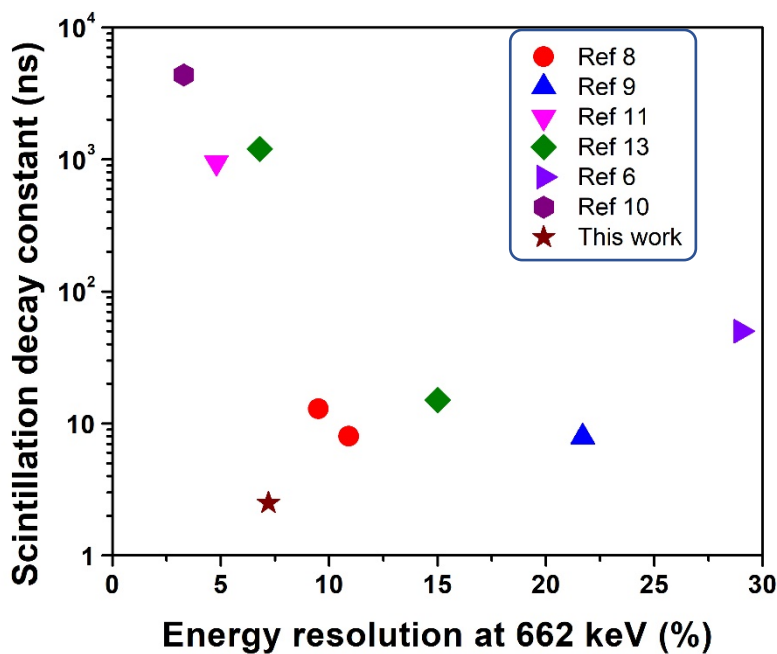

Figure 1.

Performance summary of scintillators used for gamma spectroscopy. Diagram of scintillation decay constant and energy resolution at 662 keV for the reported scintillators.

Since no individual inorganic crystals can simultaneously meet all the requirements for fast gamma spectroscopy, composite scintillators have attracted attention in recent years.[13, 14] Plastic scintillators are of particular interest due to their ultrafast scintillation decay. To make plastic scintillators useful to gamma spectroscopy, both high-Z organometallics and nanoparticles (NPs) have been studied and incorporated into plastics.[13-18] Rupert et al. used triphenylbismuth ($BiPh_3$) to enhance the photoelectric cross-section and photofraction.[13] They showed an ER of 6.8% at 662 keV with a decay constant of 1.2 μs using FIrpic as the luminescent dopant in

polyvinylcarbazole (PVK). When using 9,10-diphenylanthracene (DPA) as the dopant in polyvinyltoluene (PVT), the scintillation decay is faster at 15 ns, yet ER is lower at 9%.[13] To harness the exceptional stopping power of high-Z nanoparticles, a critical challenge is to load the NPs to a high concentration, as high as possible from the standpoint of gamma attenuation and achieve optical transparency across monolith as thick as centimeters and larger. Toda et al. reported incorporating zirconium oxide (ZrO_2) nanoparticles into plastics and achieved an average transmittance of 70% in the emission range with a 60 wt% NP loading.[18] We previously reported both non-luminescent nanoparticles and luminescent quantum dots in PVT as a nanocomposite scintillator.[16, 17] The monoliths showed a high transmittance of 65-70 % in the emission range at high-Z sensitizer loading up to 60 wt%.[16, 17] However, the volume of these nanocomposites was relatively small (≤ 0.15 cm^3), which limited their gamma stopping power and photofraction. Here we report a nanocomposite system using hafnium oxide nanoparticles (HfO_2 NPs) as the high-Z sensitizer and scale up the nanocomposites to a centimeter scale. High weight fraction (0.69) of the high-Z element (Hf) in the NPs and high density of the NPs (9.7 g/cm^3) translates to high gamma stopping power. In addition, hafnium has negligible natural radioactivity background, making it ideal for gamma spectroscopy.[1] To overcome the photoelectric energy loss in the NPs, conjugated organic compounds such as dimethylfluorene may be added in the polymer matrix to boost the overall light output.

Experimental Section

Materials

Methylstyrene (namely, vinyltoluene, 60% meta, 40% para and 1% ortho), divinylbenzene (DVB, technical grade, 80%), oleyl amine (OAm, technical grade, 70%), bis(2-(methacryloyloxy)ethyl) phosphate (BMEP), PBD ($\geq$99%), POPOP (scintillation grade), Luperox 231 (92%) and inhibitor remover (Al_2O_3) were purchased from Sigma-Aldrich. Hafnium (IV) chloride (99%) was purchased from Acros Organics. 9,9-dimethyl-9H-fluorene (MF, 97%) was purchased from Synthonix. Trifluoroacetic acid (TFA) was purchased from EMD Millipore Corporation. Chloroform ($\geq$99.8%) and lauoryl peroxide (99%) were purchased from Thermo Scientific. Ethanol, acetone and toluene (ACS grade) were purchased from Fisher Chemical. VT and DVB were eluted through an Al_2O_3-filled column to remove inhibitors, followed by degassing in liquid nitrogen. All other materials were used as received.

Synthesis of HfO$_2$ NPs

HfO_2 NPs were synthesized based on a protocol in literature with minor modification. [19] In a typical synthesis, 30 mmol $HfCl_4$ was dissolved in 50 ml TFA and stirred at 40 ˚C overnight. Unreacted TFA was removed using rotary evaporation and the resulting white solid ($Hf(TFA)_4$) was completely dried in the vacuum. 10 mmol $Hf(TFA)_4$ was subsequently dissolved into 100 ml OAm and the mixture was heated to 340˚C for 30 min under argon atmosphere. The NPs were obtained using centrifugation and purified several times using ethanol and acetone. The purified NPs were redissolved in toluene as stock solution. Typical overall yield of the reaction was 95%.

Synthesis of HfO₂ NPs loaded nanocomposites

The pristine OAm ligand was partially exchanged by BMEP based on a literature protocol with minor modification.[17] Excess BMEP was washed off and NPs were completely dried before being transferred into a nitrogen-filled glovebox where they were dispersed in VT/DVB. Peroxide initiators, MF, PBD, POPOP were co-dissolved into the solution. The curing solution was then transferred into a glass vial and sealed with a plastic lid. The nanocomposites were cured at 45-110 ˚C for a week. The resulting nanocomposites were demolded, ground and optically polished to the desired thickness and used for further characterization.

Characterization

TEM images were taken using an FEI T12 high resolution EM. Powder X-ray diffraction (XRD) pattern was taken using a Bruker PanPowder X-ray diffractometer under Cu Kα irradiation. Fourier transform infrared (FTIR) spectrum was taken using an Agilent 660 FTIR spectrometer. Thermogravimetric analysis curve was recorded on a PerkinElmer Diamond thermogravimetric/differential thermal analyzer. The samples were heated to 850˚C in air and kept there for another 10 min for complete decomposition. The nanocomposite was etched by gallium ion beam using Nova 600 SEM/FIB system to expose the cross-section and transferred to a TEM grid for imaging. The UV-Vis transmittance curves were obtained using a Shimadzu UV-1700 spectrophotometer. The nanocomposites were mounted onto a clean glass slide using optical grease and measured against a reference glass slide. A parallel measurement revealed a sample standard deviation of 0.4%. The transmission-mode PL spectra were taken in a home-built setup with an excitation wavelength of 300 nm. Microhardness was measured using a LECO LM800AT microhardness tester equipped with a Vickers indenter. The indenter dwelled on the sample for 10 s with 50 gf force before being removed. Seven indentations were made on different spots on a single sample.

Gamma scintillation measurement

We recorded the 137Cs pulse height spectra according to our previous publication.[20, 21] Briefly, the sample was placed in a Teflon holder, where it was coupled to a Hamamatsu R878 PMT using optical grease. The signals were recorded by a Canberra Lynx multichannel analyzer with a rise time of 1 μs and a flat top time of 0.5 μs. For the energy proportionality test, the sample was wrapped in several layers of Teflon and coupled with optical grease to a Hamamatsu 1294a photomultiplier tube. The PMT output was fed directly to a Tektronix 7404b oscilloscope. The collected oscilloscope pulses were then summed from 10 ns before the pulse until well past the decaying tail of each pulse. Gaussian fits around the centroid of the full-energy peaks were performed to identify the peak position in the pulse height spectra. The light output was calculated according to our previous publication. [20, 21] The Compton edge channel number of the sample from the ^{137}Cs pulse height spectra was compared to that of EJ-212 with a known light output of 10,000 ph/MeV in the same measurement conditions, followed by PMT spectral quantum efficiency correction. A parallel measurement revealed a light output standard deviation of around 100 ph/MeV after PMT spectral correction.

Scintillation decay measurement

We measured the scintillation decay time using TCSPC method with a ^{137}Cs source according to our previous publication.[20, 21] A bare terminated 800 μm multimode optical fiber was inserted onto the sample lateral through a hole in the sample holder to transmit single photon signals to the stop PMT. Both PMT outputs were fed to a Picoscope Model 5244B oscilloscope and digitized. The data acquisition time window was set to 50 ns before the pulse until well past the decaying tail of each pulse. The scintillation decay time was then calculated by fitting the curve to a single exponential decay function.

Results and Discussion

Synthesis of hafnium oxide nanoparticles loaded nanocomposites

Hafnium oxide nanoparticles were synthesized using a solvothermal method according to literature protocol at the scale of two grams of product per batch.[19] Pre-dried hafnium trifluoroacetate (Hf(TFA)$_4$) was dissolved into oleyl amine and heated at 340˚C for 30 min under argon atmosphere. The inorganic yield is 95 %, which simplifies the subsequent purification and allows even larger scale synthesis. The freshly prepared nanoparticles were carefully washed using ethanol and acetone to remove residues which could affect the clarity of the nanocomposites. The nanoparticles were dissolved in toluene to afford transparent colorless solutions. TEM images **(Figure 2a)** showed that HfO$_2$ NPs had a spherical to ellipsoid shape, with an average diameter of 4.2±0.9 nm (**Figure S1a**). FTIR spectrum (**Figure 2b)** showed multiple peaks around 1560-1650 cm^{-1} and a sharp peak at 1080 cm^{-1}, which were attributed to N-H vibration in the amine group and C-N vibration, respectively. Besides, minor peaks at 2923 cm^{-1} and 2852 cm^{-1} were attributed to C-H vibration in the methylene group. These peaks confirm that oleyl amine was present as the surface ligand. The XRD pattern of HfO$_2$ NPs **(Figure 2c)** was aligned with the standard pattern of HfO$_2$ (PDF# 43-1017, monoclinic, P2$_1$/c). The broadened peaks indicated nanocrystalline nature of the resulting HfO$_2$. TGA curve of HfO$_2$ NPs **(Figure 2d)** showed a normalized residue weight at 850˚C of 0.83, indicating the oleyl amine ligand made up 17 wt% in HfO$_2$ NPs. The surface coverage of the NPs with OAm was estimated to be 3.2 molecules/nm^2 from TGA and TEM results (See details in Supporting Information). Half of the pristine oleyl amine ligand was subsequently replaced with bis(2-(methacryloyloxy)ethyl) phosphate (BMEP), rendering the nanoparticle capability to be co-polymerized with vinyl monomers.[17] The resulting NPs were washed with acetone and dried in vacuum for subsequent use.
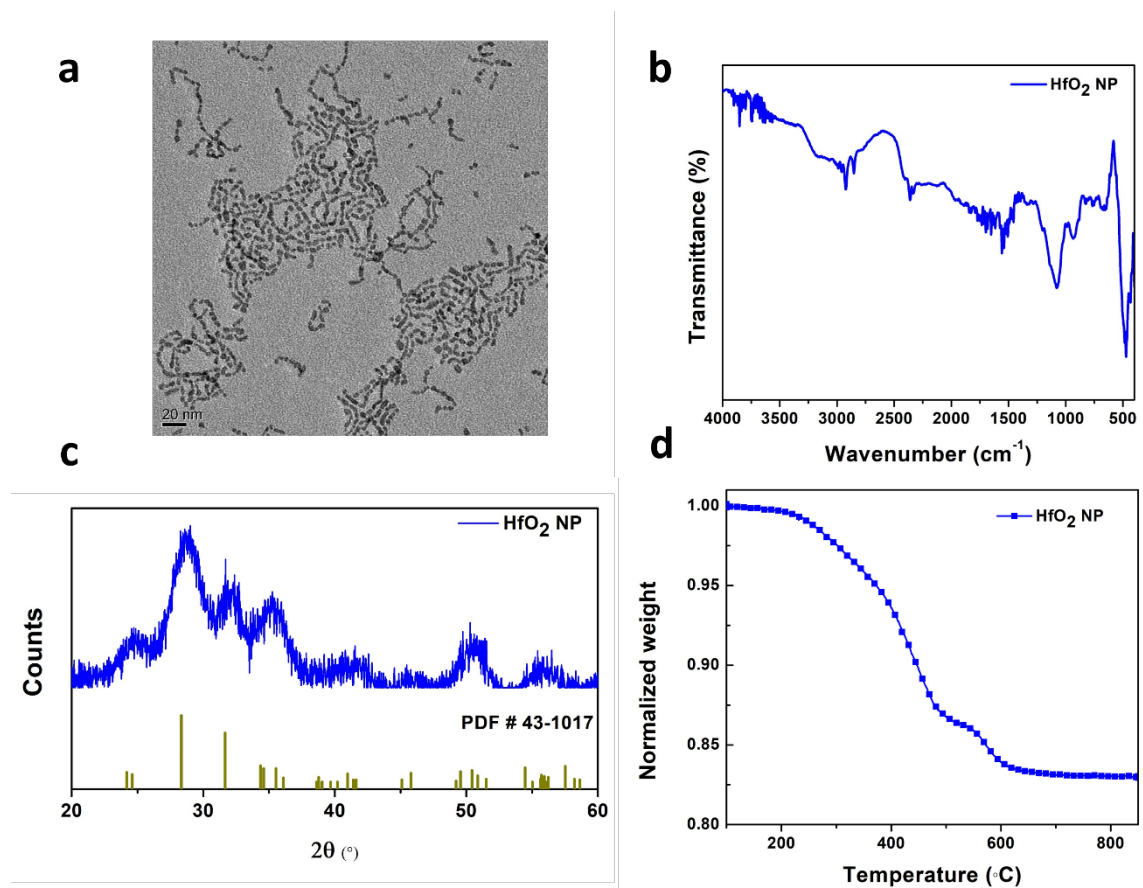
Figure 2. Characterization of HfO₂ NPs (wrapped with oleyl amine ligand).

(a) TEM image. (b) FTIR spectrum. (c) XRD pattern of the NPs and standard pattern of HfO₂ (PDF# 43-1017) (d) TGA curve taken in air.

Vinyltoluene (VT), HfO₂ NPs, 9,9-dimethyl-9H-fluorene (MF), 2-(4-Biphenylyl)-5-phenyl-1,3,4-oxadiazole (PBD), 1,4-Bis(5-phenyl-2-oxazolyl)benzene (POPOP), divinylbenzene (DVB) and peroxide initiators were mixed in a nitrogen-filled glovebox to afford transparent colorless dispersions. The solutions were transferred to sealed glass vials and loaded onto an aluminum heating block for curing. During curing, solutions containing 20 wt% and 40 wt% NPs became viscous and solidified much more quickly than their unloaded counterparts. This is because high loadings of NPs contributed to a significantly higher crosslinker activity (an additional 2-4 wt%) as the NPs were modified with a bi-methacrylate functionalized ligand. The NP-loaded solutions turned pale white yet still transparent in the first few hours and subsequently became colorless as the methacrylate-terminating nanoparticles began to copolymerize with VT. After curing at 45-95 ˚C for five days, the glass vials were broken to demold the solidified nanocomposites. We noticed that it was difficult to demold nanocomposites when NPs were added. This is probably because less curing extent was accomplished in those nanocomposites as they arrived at their gel point much earlier, resulting in sluggish diffusion of the remaining monomers under the same

7

conditions.[22] To compensate for the lower curing extent, the nanocomposites containing NPs were post-cured at 110 ˚C before being demolded.

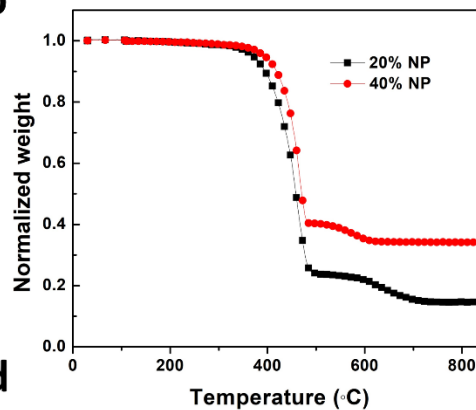**Composition and optical properties of the nanocomposites**

Figure 3a shows nanocomposites containing 0, 20, and 40% HfO$_2$ NPs (thickness=2 mm) and the rightmost is an 8.5 mm-thick nanocomposite containing 40% NPs. TGA curves of the nanocomposites (**Figure 3b**) showed a residual weight at 850 ˚C of 0.15 and 0.34 for 20% and 40% NPs loaded nanocomposites, respectively. The residual weight represented the actual NP loading (excluding ligand) and agreed well with their respective pre-determined loading (including ligand) given the instrument error. To examine the NPs dispersion in the plastics, we etched a nanocomposite with 20% NPs using a gallium ion beam to expose its cross-section and transferred it to a TEM grid for imaging. TEM image of the cross-section of the etched film showed an average diameter of 4.6±0.9 nm (**Figure 3c** and **Figure S1b**). The particle size barely changed compared to its colloidal counterpart. There were a few NP clusters (20-40 nm) present, probably because of the NPs polymerization with their adjacent counterparts. However, the particles were distanced from each other within the clusters, thus not affecting bulk transmittance.
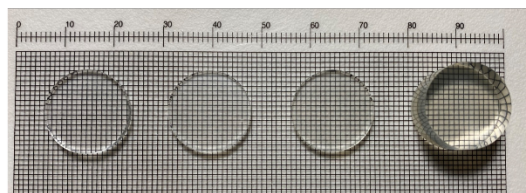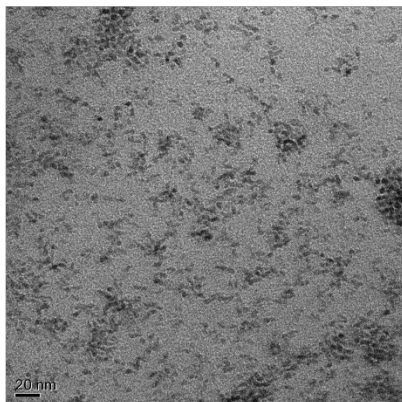
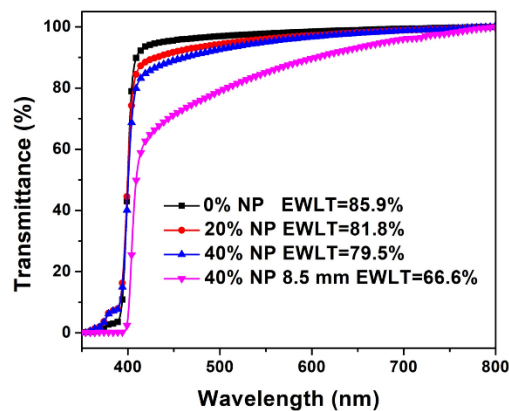**Figure 3. Composition and optical properties of the nanocomposites.** (a) Photograph of nanocomposites loaded with HfO_2 NPs with a thickness of 2 mm. From left to right: 0% NP, 20% NP, 40% NP, 40% NP (8.5 mm thickness). (b) TGA curves. (c) TEM image of an etched film of a nanocomposite loaded with 20% NPs. (d) Transmittance curves and EWLT values.

Bulk transmittance is the key to high scintillation light output. **Figure 3d and S2** show the transmittance curves and photoluminescence (PL) spectra for nanocomposites containing 0-40% NPs and 20% MF. Emission weighted longitudinal transmittance (EWLT) was calculated to quantify the bulk transmittance of a nanocomposite to its own scintillation light.[23] All 2 mm-thick nanocomposites showed high EWLT, which only slightly decreased with increased NP loadings, indicating minor Rayleigh scattering due to the addition of NPs. Compared to a commercial scintillator, EJ-212, of which the EWLT is 92.2%,[24] the unloaded nanocomposite (0% NP+20% MF) showed a lower EWLT of 85.9%. This is due to the formation of crystalline MF aggregates, which scattered the light.[20] We also found that crosslinker (i.e. DVB) played an important role in bulk transmittance. **Figure S3** showed the transmittance curves of two nanocomposites containing 20% NPs and 20% MF of the same thickness. The EWLT significantly increased from 55.2% to 81.8% when the DVB amount increased from 2 vol% to 5 vol%. This may be attributed to the interchain spacing increase, thus reducing packing density and scattering.[25, 26] However, the 8.5 mm-thick nanocomposite had a notably lower EWLT (66.6%) due to aggravated scattering in the longer light path as was suggested by a 2.5 nm redshift in its peak emission wavelength. (**Figure S2**) The PL spectra were recorded in a transmission geometry where the incident light hit the nanocomposites from one side while the spectrometer sat at the other side along the incident direction. All 2 mm-thick nanocomposites showed identical PL characteristics, further indicating minor scattering introduced by the addition of NPs.

Gamma response and scintillation decay time

We reported the use of MF in plastic scintillators to enhance exciton production and transfer efficiency.[20] Hence, we first examined the MF effects in light output in the scaled-up nanocomposites (diameter: 17 mm). We prepared monoliths containing 0-30% MF and 0% NPs and the light output reached a maximum of 10363 ph/MeV at 20% MF loading (**Figure S4**). Transmission-mode PL spectra (**Figure S5**) showed that emission characteristics barely changed with MF loading, indicating light output enhancement resulted from the actual enhancement in exciton production/transfer efficiency instead of PMT spectral correction. Therefore, we used 20% MF loading (absolute) for all nanocomposites. Nanocomposites loaded with 20% and 40% NPs were prepared with a thickness of 2 mm. The ^{137}Cs gamma pulse height spectra (**Figure 4a**) showed a light output of 9191 ph/MeV at 20% NP loading. The light output was 7822 ph/MeV at 40% loading (net 24 wt% Hf), which was 1.5 times of that of EJ-256, a commercial plastic scintillator with lead loading (5 wt% Pb).[27] A photopeak showed up at 20% NP loading and became prominent at 40% loading. The energy resolved pulse height spectrum of the 40% NP

nanocomposite (**Figure 4b**) showed a deconvoluted photopeak with an energy resolution of 7.2% at 662 keV. The fluorescence X-ray peak was also shown, but the peak position (22 keV) was distorted due to the small scintillator volume.
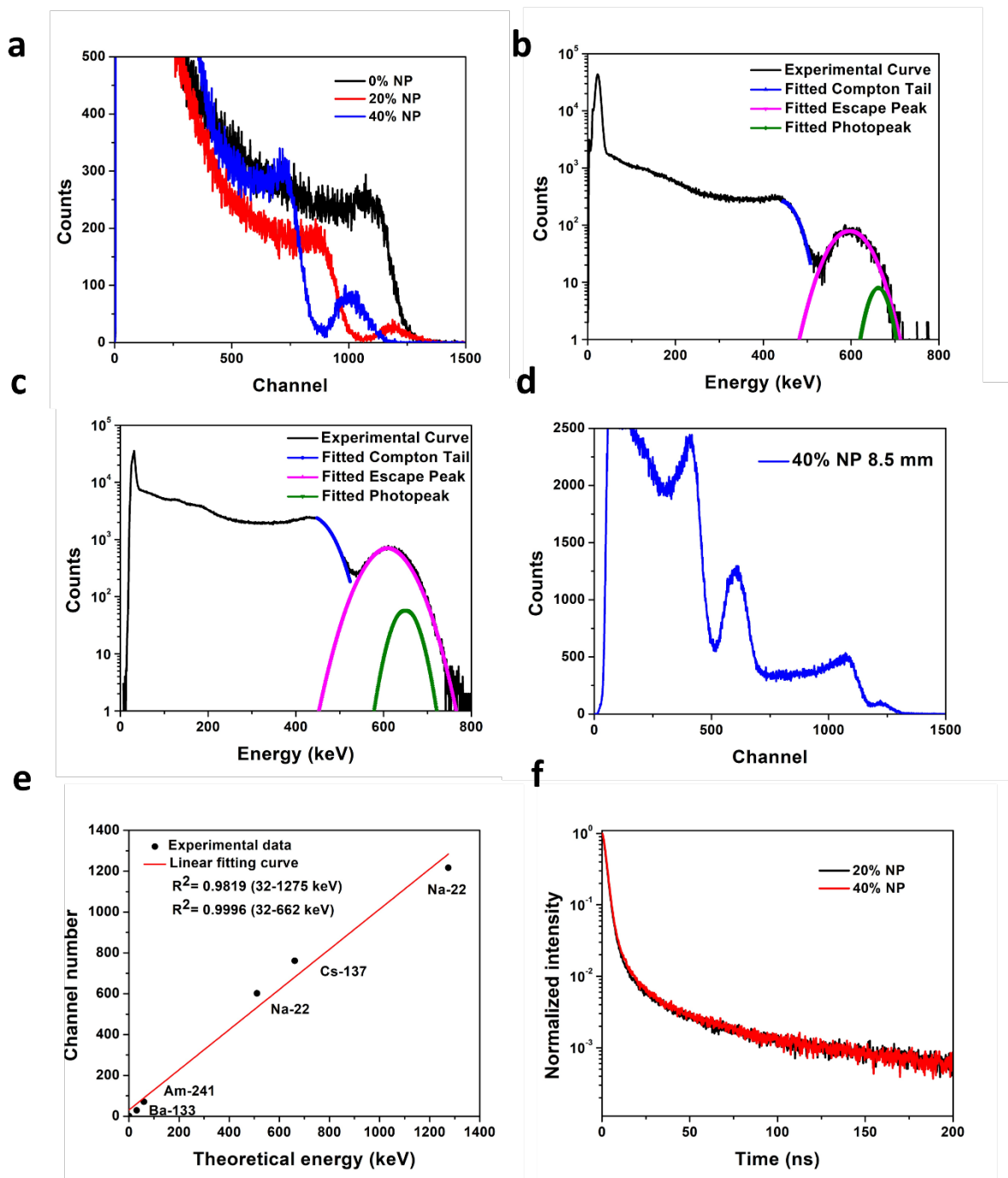
Figure 4. Gamma scintillation properties. (a) ^{137}Cs pulse height spectra of nanocomposites (2 mm thickness) loaded with 0-40% HfO$_2$ NPs. (b) Energy resolved spectrum of the nanocomposite loaded with 40% HfO$_2$ NPs (2 mm thickness) with escape peak and photopeak

deconvoluted. (c) Energy resolved spectrum of a nanocomposite loaded with 40% HfO_2 NPs (8.5 mm thickness). (d) ^{22}Na pulse height spectrum of the nanocomposite loaded with 40% HfO_2 NPs (8.5 mm thickness). (e) Linear fitting plot of the measured photopeak channel values as a function of theoretical incident energy values for the nanocomposite loaded with 40% HfO_2 NPs (8.5 mm thickness). (f) ^{137}Cs scintillation decay curves of nanocomposites loaded with 20% and 40 % HfO_2 NPs (2 mm thickness).

To acquire better photofraction, we scaled up the 40% NP nanocomposite to 8.5 mm thickness. The light output slightly decreased to 7197 ph/MeV because of bulk transmittance loss. The energy resolved pulse height spectrum (**Figure 4c**) showed a deconvoluted photopeak with an energy resolution of 9.1% at 662 keV. The energy resolution deterioration was attributed to decreased light output. However, the 32 keV fluorescence X-ray peak was clearly resolved as a result of enhanced gamma stopping power. The 511 keV and 1275 keV photopeaks were both present in the pulse height spectrum using ^{22}Na source. (**Figure 4d**) This further demonstrates excellent gamma stopping power of the nanocomposite as a synergistic result of high NP loading and a large volume. To assess the energy proportionality of the nanocomposites, pulse height spectra were acquired on the 8.5 mm-thick nanocomposite using several radioactive isotopes emitting gamma rays covering a broad range of energies. The isotopes and energy peaks used were ^{133}Ba (31 keV), ^{241}Am (60 keV), ^{22}Na (511keV/1275 keV), ^{137}Cs (662 keV). **Figure 4e** shows the photopeak channel values plotted against their theoretical energy values. It shows an energy proportionality within 32-662 keV with a linear correlation coefficient of 0.9996. However, it deteriorated at 1275 keV gamma with a linear correlation coefficient of 0.9815. We note that a different amplifier gain and offset on the oscilloscope were used to accommodate the higher energy measurements of the 1275 keV gamma. This change may affect the compensation of the oscilloscope and thus the resulting peak positions. The non-zero y-intercept arised from the electronic noise in the readout circuit. The good energy proportionality in the range of 32-662 keV is attributed to the high stopping power and light output of the nanocomposite.

Scintillation decay time is another key property for scintillators. Of all commercial scintillation dyes, we chose POPOP as the final emission dye for its ultrafast fluorescence decay time (1.1 ns in cyclohexane)[28] and its high PL quantum efficiency (PLQY=0.97 in cyclohexane).[29] We reported that the addition of MF did not alter the fast decay of plastic scintillators as MF participated in an even faster Förster resonance energy transfer (FRET) process in the cascade energy transfer.[20] Herein, we further studied the scintillation decay time of 20% and 40% NP loaded nanocomposites using a time correlated single photon counting (TCSPC) method. Both curves showed a predominantly single exponential decay, indicating that the scintillation light solely came from POPOP fluorescence. The characteristic decay time is 2.4 ns for the 20% NP nanocomposite and 2.5 ns for the 40% one (**Figure 4f and Table S1**), which are very close to that of the unloaded nanocomposite (2.3 ns).[20] We conclude that the addition of NPs did not alter the fast scintillation kinetics. It is known that MF participates in the cascade energy transfer via FRET in the conjugated polymer matrix. However, it is unclear whether the NPs transferred their excitation energy to the polymer matrix.   Given that the band gap of HfO_2 NPs (6.0 eV) is much larger than that of MF (3.9 eV) or PVT (4.5 eV) and the NPs are non-luminescent, we speculate

that excitonic energy from the nanoparticles to the polymer matrix is either insignificant or of low efficiency. Therefore, we attributed the unchanged scintillation kinetics to none/negligible contribution from NPs to the cascade energy transfer.

Mechanical properties and thermal aging study

Mechanical strength and environmental stability are important for practical use. To probe the hardness of the nanocomposites, we measured microhardness using a Vickers indenter following the ASTM E 384 standard. **Figure 5a** shows the Vickers hardness number as a function of NP loading along with that of EJ-212. The unloaded nanocomposite showed a slightly lower Vickers hardness number (19.5) than EJ-212 (21.9). However, it decreased to 7.9 at 20% NP loading and further to 7.4 at 40% NP loading, but still higher than that of a non-crosslinked polystyrene (6.1), a widely used commercial plastic material.[30] Although it is counterintuitive to see microhardness deterioration as metal-oxide NPs are widely used in the polymer matrix as strengthening fillers, this only applies to the low loading regime (1-2 wt% typically).[31] When it comes to the high loading regime (>5 wt%), the abrupt deterioration is most probably due to polymer matrix embrittlement with the addition of NPs.[31]

Figure 5. Mechanical properties and thermal aging test of nanocomposite scintillators and EJ-212. (a) Vickers hardness number as a function of NP loading along with EJ-212. (b) Light output as a function of aging time of nanocomposites loaded with 20%, 40% NPs and EJ-212. Condition: 60˚C and 10% RH.

To study the environmental stability of the nanocomposites, nanocomposites containing 20% and 40% NPs along with EJ-212 were aged at 60 ˚C and ambient humidity (~10% RH) inside an environmental chamber. The light output of 20% NPs loaded nanocomposite barely changed while the 40% one only showed a minor decrease (4%) in 28 days (**Figure 5b**). The high
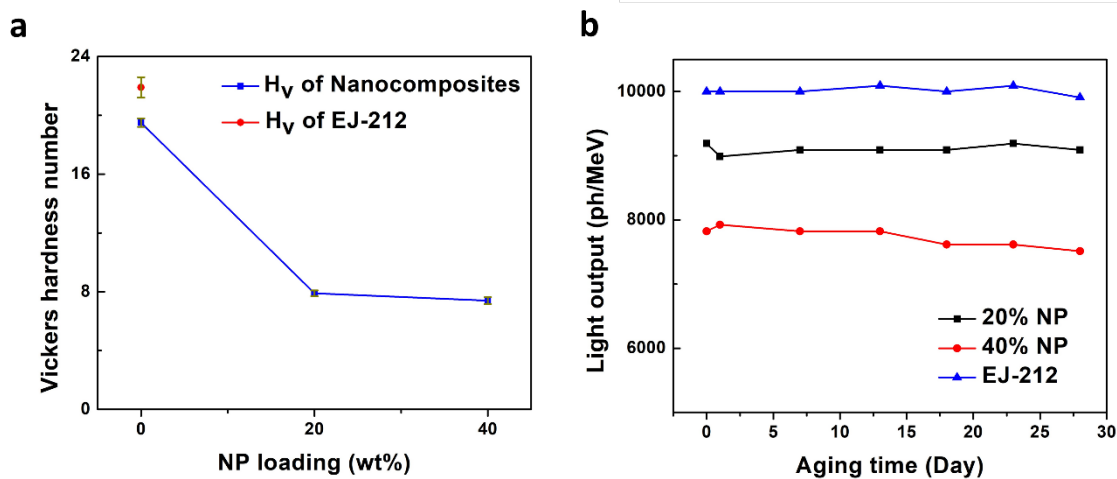
environmental stability is attributed to (1) NPs are highly stable up to 250 ºC in air (<1 wt% loss

from TGA) and (2) NPs are covalently bound to the polymer matrix preventing diffusion and avoiding nanoparticle aggregation at elevated temperature.

Conclusions

Centimeter-size nanocomposite monoliths loaded with 40% NPs have successfully been synthesized with high bulk transmittance. With MF enhancing energy transfer efficiency in the matrix, light output was improved to 1.5 times of EJ-256 with a net 24 wt% Hf loading. Energy photopeaks were well resolved in the gamma pulse height spectra of 32/662 keV for ^{137}Cs and 511/1275 keV for ^{22}Na. The nanocomposite showed good energy proportionality over from 32 to 1275 keV. To our best knowledge, this is the first time to detect a >1 MeV photopeak using a plastic-based scintillator. The energy resolution at 662 keV was determined to be 7.2% - 9.1% by peak deconvolution. The nanocomposites retained ultrafast scintillation decay time (~2 ns) of plastic scintillators. With its high environmental stability, the nanocomposite scintillators may be promising to replace conventional plastic scintillators in certain applications.

ASSOCIATED CONTENT

Supporting Information. The following file is available free of charge.
Nanoparticles size distribution, PL spectra, transmittance curves, pulse height spectra, scintillation decay constants and scintillation parameters comparison to literature data. (Word)

AUTHOR INFORMATION

Corresponding Author

Qibing Pei

Email: qpei@seas.ucla.edu

Author Contributions

The manuscript was written through contributions of all authors. All authors have given approval to the final version of the manuscript.

Funding Sources

Notes

The authors declare no competing financial interest.

REFERENCES

(1) Dujardin, C.; Auffray, E.; Bourret-Courchesne, E.; Dorenbos, P.; Lecoq, P.; Nikl, M.; Vasil'ev, A. N.; Yoshikawa, A.; Zhu, R. Y. Needs, Trends, and Advances in Inorganic Scintillators. *IEEE Trans. Nucl. Sci.* **2018**, *65*, 1977-1997.
(2) Knoll, G. F. *Radiation Detection and Measurement*; John Wiley & Sons, 2010.
(3) Moseley, O. D. I.; Doherty, T. A. S.; Parmee, R.; Anaya, M.; Stranks, S. D. Halide Perovskites Scintillators: Unique Promise and Current Limitations. *Journal of Materials Chemistry C* **2021**, *9*, 11588-11604.
(4) Lecoq, P. Development of New Scintillators for Medical Applications. *Nuclear Instruments and Methods in Physics Research Section A: Accelerators, Spectrometers, Detectors and Associated Equipment* **2016**, *809*, 130-139.
(5) Lecoq, P.; Morel, C.; Prior, J. O.; Visvikis, D.; Gundacker, S.; Auffray, E.; Križan, P.; Turtos, R. M.; Thers, D.; Charbon, E., et al. Roadmap toward the 10 ps Time-of-Flight Pet Challenge. *Physics in Medicine & Biology* **2020**, *65*, 21RM01.
(6) Kawano, N.; Koshimizu, M.; Okada, G.; Fujimoto, Y.; Kawaguchi, N.; Yanagida, T.; Asai, K. Scintillating Organic–Inorganic Layered Perovskite-Type Compounds and the Gamma-Ray Detection Capabilities. *Scientific Reports* **2017**, *7*, 14754.
(7) Di, J.; Chang, J.; Liu, S. Recent Progress of Two-Dimensional Lead Halide Perovskite Single Crystals: Crystal Growth, Physical Properties, and Device Applications. *EcoMat* **2020**, *2*, e12036.
(8) Maddalena, F.; Xie, A.; Arramel; Witkowski, M. E.; Makowski, M.; Mahler, B.; Drozdowski, W.; Mariyappan, T.; Springham, S. V.; Coquet, P., et al. Effect of Commensurate Lithium Doping on the Scintillation of Two-Dimensional Perovskite Crystals. *Journal of Materials Chemistry C* **2021**, *9*, 2504-2512.
(9) Jin, T.; Liu, Z.; Luo, J.; Yuan, J.-H.; Wang, H.; Xie, Z.; Pan, W.; Wu, H.; Xue, K.-H.; Liu, L., et al. Self-Wavelength Shifting in Two-Dimensional Perovskite for Sensitive and Fast Gamma-Ray Detection. *Nature Communications* **2023**, *14*, 2808.
(10) Burger, A.; Rowe, E.; Groza, M.; Morales Figueroa, K.; Cherepy, N. J.; Beck, P. R.; Hunter, S.; Payne, S. A. Cesium Hafnium Chloride: A High Light Yield, Non-Hygroscopic Cubic Crystal Scintillator for Gamma Spectroscopy. *Appl. Phys. Lett.* **2015**, *107*.
(11) Wang, Q.; Wang, C. e.; Wang, Z.; Sun, X.; Nikl, M.; OuYang, X.; Wu, Y. Achieving Efficient Neutron and Gamma Discrimination in a Highly Stable 6li-Loaded $Cs_3Cu_2I_5$ Perovskite Scintillator. *The Journal of Physical Chemistry Letters* **2022**, 9066-9071.
(12) Li, S.; Luo, J.; Liu, J.; Tang, J. Self-Trapped Excitons in All-Inorganic Halide Perovskites: Fundamentals, Status, and Potential Applications. *The Journal of Physical Chemistry Letters* **2019**, *10*, 1999-2007.
(13) Rupert, B. L.; Cherepy, N. J.; Sturm, B. W.; Sanner, R. D.; Payne, S. A. Bismuth-Loaded Plastic Scintillators for Gamma-Ray Spectroscopy. *Europhys. Lett.* **2012**, *97*, 22002.

(14) Bertrand, G. H. V.; Dumazert, J.; Sguerra, F.; Coulon, R.; Corre, G.; Hamel, M. Understanding the Behaviour of Different Metals in Loaded Scintillators: Discrepancy between Gadolinium and Bismuth. *Journal of Materials Chemistry C* **2015**, *3*, 6006-6011.

(15) Cherepy, N. J.; Sanner, R. D.; Beck, P. R.; Swanberg, E. L.; Tillotson, T. M.; Payne, S. A.; Hurlbut, C. R. Bismuth- and Lithium-Loaded Plastic Scintillators for Gamma and Neutron Detection. *Nuclear Instruments and Methods in Physics Research Section A: Accelerators, Spectrometers, Detectors and Associated Equipment* **2015**, *778*, 126-132.

(16) Chen, Y.; Liu, C.; Jin, Y.; Hajagos, T.; Kishpaugh, D.; Zhuang, Q.; Pei, Q. *Ytterbium Fluoride Loaded Plastic Scintillators for Γ-Ray Spectroscopy*; SPIE, 2016.

(17) Liu, C.; Li, Z.; Hajagos, T. J.; Kishpaugh, D.; Chen, D. Y.; Pei, Q. Transparent Ultra-High-Loading Quantum Dot/Polymer Nanocomposite Monolith for Gamma Scintillation. *ACS Nano* **2017**, *11*, 6422-6430.

(18) Toda, A.; Kishimoto, S. X-Ray Detection Capabilities of Plastic Scintillators Incorporated with Zro2 Nanoparticles. *IEEE Trans. Nucl. Sci.* **2020**, *67*, 983-987.

(19) Zhao, H.; Yu, H.; Redding, C.; Li, Z.; Chen, T.; Meng, Y.; Hajagos, T. J.; Hayward, J. P.; Pei, Q. Scintillation Liquids Loaded with Hafnium Oxide Nanoparticles for Spectral Resolution of Γ Rays. *ACS Applied Nano Materials* **2021**, *4*, 1220-1227.

(20) Han, Z.; Yu, H.; Pei, Q. Fluorene Derivatives for Efficient Prompt Scintillation in Plastic Scintillators. *ACS Applied Polymer Materials* **2022**, *4*, 4424-4431.

(21) Yu, H.; Chen, T.; Han, Z.; Fan, J.; Pei, Q. Liquid Scintillators Loaded with up to 40 Weight Percent Cesium Lead Bromide Quantum Dots for Gamma Scintillation. *ACS Applied Nano Materials* **2022**, *5*, 14572-14581.

(22) Basile, L. J. Effect of Styrene Monomer on the Fluorescence Properties of Polystyrene. *The Journal of Chemical Physics* **2004**, *36*, 2204-2210.

(23) Zhu, R.-Y. Ultrafast and Radiation Hard Inorganic Scintillators for Future Hep Experiments. In *Journal of Physics: Conference Series*, 2019; IOP Publishing: p 012022.

(24) Yu, H.; Zhao, R.; Redding, C.; Chen, T.; Hajagos, T.; Ferrelli, G.; Zaldivar, R.; Hayward, J.; Pei, Q. *Organic Liquid and Nanocomposite Scintillators for Gamma Spectroscopic Detections*; SPIE, 2021.

(25) Jeong, K.-M.; Li, Y.; Yoo, D.-G.; Lee, N.-K.; Lee, H.-G.; Ando, S.; Ha, C.-S. Effects of Crosslinking Agents on the Physical Properties of Polyimide/Amino-Functionalized Graphene Oxide Hybrid Films. *Polym. Int.* **2018**, *67*, 588-597.

(26) Hajagos, T. J.; Garcia, E.; Kishpaugh, D.; Pei, Q. Plastic Scintillators Based on Thermally Activated Delayed Fluorescence Dyes. *Nuclear Instruments and Methods in Physics Research Section A: Accelerators, Spectrometers, Detectors and Associated Equipment* **2019**, *940*, 185-198.

(27) *Ej-256 - Lead Loaded Plastic Scintillator - Eljen Technology*. https://eljentechnology.com/products/plastic-scintillators/ej-256 (accessed 2023 September 2).

(28) Boens, N.; Qin, W.; Basarić, N.; Hofkens, J.; Ameloot, M.; Pouget, J.; Lefèvre, J.-P.; Valeur, B.; Gratton, E.; vandeVen, M., et al. Fluorescence Lifetime Standards for Time and Frequency Domain Fluorescence Spectroscopy. *Anal. Chem.* **2007**, *79*, 2137-2149.

(29) Berlman, I. *Handbook of Fluorescence Spectra of Aromatic Molecules*; Academic Press, 2012.

(30) Katare, R.; Bajpai, R.; Datt, S. C. Microhardness of Blends of Polystyrene and Poly(Methyl Methacrylate). *Polym. Test.* **1991**, *10*, 139-143.

(31) Nielsen, L. E.; Landel, R. F. *Mechanical Properties of Polymers and Composites / Lawrence E. Nielsen, Robert F. Landel*; M. Dekker, 1994.

TOC graphic

Luminescent PVT matrix

Gamma ray

Ligand

HfO$_2$ NP

Medical Imaging

Nuclear Security